



1 **Synergistic effect of water-soluble species and relative humidity on**
2 **morphological changes of aerosol particles in Beijing mega-city during**
3 **severe pollution episodes**

4 Xiaole PAN¹, Baozhu GE¹, Zhe WANG^{1,2}, Yu TIAN^{1,3}, Hang LIU^{1,3}, Lianfang WEI¹, Siyao YUE^{1,3},
5 Itsushi UNO², Hiroshi KOBAYASHI⁴, Tomoaki NISHIZAWA⁵, Atsushi SHIMIZU⁵, Pingqing FU^{1,3,7},
6 Zifa WANG^{1,3,6},

7 ¹State Key Laboratory of Atmospheric Boundary Layer Physics and Atmospheric Chemistry, Institute of Atmospheric Physics,
8 Chinese Academy of Sciences, Beijing, 100029, China

9 ²Research Institute for Applied Mechanics, Kyushu University, Kasuga, 816-8580, Japan

10 ³University of Chinese Academy of Sciences, Beijing, 100049, China

11 ⁴University of Yamanashi, Yamanashi, 400-0016, Japan.

12 ⁵National Institute for Environmental Studies, Ibaraki, 305-8506, Japan

13 ⁶Center for Excellence in Regional Atmospheric Environment, Institute of Urban Environment, Chinese Academy of
14 Sciences, Xiamen 361021, China

15 ⁷Institute of Surface-Earth System Science, Tianjin University, Tianjin, 300072, China

16

17 *Correspondence to:* Xiaole PAN (panxiaole@mail.iap.ac.cn)

18 **Abstract.** Depolarization ratio (δ) of backscattered light from aerosol particle is an applicable parameter for real-time
19 distinguishing spherical and non-spherical particles, which has been widely adopted by ground-based Lidar observation and
20 satellite remote sensing. From November 2016 to February of 2017, it consecutively suffered from numbers of severe air
21 pollution at Beijing with daily averaged mass concentration of $PM_{2.5}$ (aerodynamic diameter less than $2.5\mu m$) larger than 150
22 $\mu g/m^3$. We performed concurrent measurements of water-soluble chemical species and depolarization properties of aerosol
23 particles on the basis of a continuous dichotomous Aerosol Chemical Speciation Analyzer (ACSA-14) and a bench-top optical
24 particle counter with a polarization detection module (POPC). We found that δ value of ambient particles generally decrease
25 as mass concentration of $PM_{2.5}$ increased at unfavorable meteorological condition. Ratio of mass concentration of nitrate
26 (NO_3^-) to that of sulfate (SO_4^{2-}) in $PM_{2.5}$ was 1.5 ± 0.6 , indicating of great importance of NO_3 in the formation of heavy
27 pollution. Mass concentration of NO_3^- in $PM_{2.5}$ (fNO_3) was generally an order of magnitude higher than that in coarse mode



28 (cNO₃) with a mean fNO₃/cNO₃ ratio of 14 ± 10 . Relatively high allocation (fNO₃/cNO₃ = 5) of NO₃⁻ in coarse mode could
29 be partially attributed to hygroscopic growth/coagulation of nitrate-rich fine mode particles under higher relative humidity
30 condition. As a result, δ values of particles with $D_p = 2 \mu\text{m}$ ($\delta_{D_p=2}$) and $5 \mu\text{m}$ ($\delta_{D_p=5}$) decreased evidently as the mass fraction
31 of water-soluble species (NO₃⁻ and SO₄²⁻) increase in both PM_{2.5} and PM_{2.5-10}, respectively. In particular, due to synergistic
32 effect of RH, $\delta_{D_p=5}$ value could decrease by 50% as mass fraction of NO₃⁻ in PM_{2.5-10} increased from 8% to 23%. It suggested
33 that alteration of non-sphericity of mineral dust particles was evident owing to coating with pollutants and heterogeneous
34 reactions on the surface of the particle during heavy pollution period. This study brings the attention to great variability of
35 morphological changes of aerosol particles along the transport, which have great complex effects in evaluating their climate
36 and health effect.

37 **1 Introduction**

38 Tropospheric aerosols, in particular the particles with aerodynamic diameter less than $2.5 \mu\text{m}$ (PM_{2.5}), have detrimental impact
39 on human health. It degrades the air quality by increasing atmospheric turbidity, and affects regional/global climate by
40 disturbing the solar radiation transfer in the Earth system via scattering/absorbing light directly and altering amount and
41 lifespan of cloud (Ramanathan et al., 2001; Kaufman et al., 2002). In the past decades, intensive anthropogenic/industrial
42 activities in East Asia emit huge amount of primary pollutants such as SO₂, NO_x, NH₃, VOCs etc., which resulted in severe
43 air pollution. PM_{2.5} was mainly composed of light-scattering species (sulfate, nitrate, ammonium, organics etc.) and light-
44 absorbing matter (BC, BrC etc.). Under high relative humidity condition, most of aerosol particles absorb water vapor and
45 undergo apparently hygroscopic growth, which lead to dramatic changes in its mass concentration, size distribution, optical
46 properties (single scattering albedo etc.), as well as its corresponding morphologies. For example, freshly emitted rBC particles
47 were normally in a chain-like aggregates with visible carbon monomers, and they are sometimes fully coated or partially
48 coated by organics/inorganic matters. Due to atmospheric aging processes in polluted areas at high relative humidity rBC core
49 tend to shrink to a compact one with apparent non-refractory coatings, and its light-absorbing capacity for thickly coated rBC
50 also increased by a factor of 2.

51 Mineral aerosol is also one of the key compounds in East Asia, it was frequently reported to be coated by anthropogenic
52 pollutants along its transport owing to heterogeneous reactions with reactive acidic gas and coagulation of soluble particles.
53 In polluted area, photo-chemically formatted nitric acid (HNO₃) could easily react with CaCO₃ to form Ca(NO₃)₂ on the
54 surface of dust particles. The consecutive water-absorbing process will also lead to apparent morphological changes of dust
55 particles, which also impact on dust-cloud interaction (Tian et al., 2018) and new particle formation etc. Till now, online
56 investigation on the morphological changes of aerosol particle in the ambient environment is still limit. The widely-adopted
57 method to study the morphology and mixing state of particles is filter-based single particle sampling with electron-microscopy
58 inspection in laboratory. For example, scanning electron microscopy (SEM) coupled with energy dispersive X-ray
59 spectrometry (EDX) could provide information about surface topography, composition of the sample surface by scanning it
60 with a high-energy beam of electrons. Li et al., (2009) using Transmission electron microscopy (TEM) found that approximate



61 90% of sampled mineral particles were covered by visible nitrate coatings during pollution episode in Central East China. As
62 a matter of fact, such hygroscopic coating on some individual dust particles was observed not only in polluted area but also at
63 clean marine area. The observation on R/V during ACE-Asia found that dust particles mixed with chloride was sometimes
64 dominant over sulphate and nitrate due to disassociation of acidified sea salt particles (Sullivan et al., 2007). Tobo et al.,
65 (2010) found that Asian dust particles could also be deliquescent to aqueous droplet as a result of formation of CaCl_2 . Dust
66 particle could also acquire sulphate coatings via either heterogeneous uptake of gaseous SO_2 and subsequent oxidation or
67 coagulation within cloud or fog droplets (Kojima et al., 2006), as well as volatile carbonaceous species due to condensation
68 processes (Kim and Park, 2012). Although diversity in chemical composition and structure of single particles with different
69 degree of aging were investigated in the past studies (literatures), these analyses had to be inspected objectives one by ones,
70 and such labor intensive operation cause difficult in broadening the results due to poor statistics (Li et al., 2009).

71 To obtain better understanding the real-time morphological variation of atmospheric processing particles, polarization
72 property of backscattering light from the illuminated particle has been used as an applicable surrogate. For spherical particle,
73 oscillation direction of magnetic wave of scattering light was identical to the incident light. Therefore, depolarization ratio
74 (DR, here defined as the ratio of *s*-polarized to *p*-polarized backward component) was zero theoretically. However, for
75 uncoated dust particles, the direction deviates significantly with a large DR value. Such characteristic is widely used to
76 distinguish dust and spherical particles by both ground-based Lidar observation (Asian Dust and Aerosol Lidar Observation
77 Network, AD-Net) (Müller et al., 2007; Thorsen et al., 2016; Hofer et al., 2017) and satellite on-board remote sensing (Cloud-
78 Aerosol Lidar with Orthogonal Polarization on-board the CALIPSO) (Winker et al., 2010; Yu et al., 2015; Geng et al., 2011)
79 presuming that spherical particles and dust were externally mixed. On the basis of this technique, studies on spatial-resolved
80 distribution (Hara et al., 2008; Uno et al., 2008), transport pattern (Uno et al., 2009) of pollution and dust, and data processing
81 algorithm (Nishizawa et al., 2007; Winker et al., 2009; Nishizawa et al., 2011) have been widely performed. For instance,
82 Shimizu et al. (2004) summarized the contributions of different aerosol types on the total backscattering coefficient at multiple
83 sites in East Asia using three-channel Mie scattering Lidar data. Huang et al. (2015) identified anthropogenic dust particles due
84 to human activities and its contribution to global dust loading on the basis of CALIPSO observation. Recently, a multi-
85 wavelength Mie-Raman Lidar (MMRL) and a new algorithm were developed to estimate extinction coefficients for black
86 carbon, dust, sea salt, and air-pollution aerosols (a mixture of sulfate, nitrate and organic carbon substances) (Hara et al.,
87 2017; Nishizawa et al., 2017).

88 It was worth noting that atmospheric particles were normally internally mixed. Once the dust particles were coated by other
89 water-soluble pollutants, its polarization degree may decrease. Therefore, it is a challenge to accurately classifying in
90 coated/uncoated dust particles due to its morphological diversity. In particular, Lidar adopted a volume depolarization ratio to
91 discriminate different aerosol types; it was easily biased due to presence of small spherical particles in the volume of targeted
92 air volume. To overcome this shortcoming, recently a bench-top optical particle counter equipped with a depolarization
93 module (Polarization Optical Particle Counter) was developed to detect the size-resolved polarization of individual particles.



94 POPC is capable of investigating the temporal variation of mixing state of single dust particles. The observation at an urban
95 site in Japan showed that DR of super-micron particles decreased evidently due to an increase of mass fraction of nitrate
96 concentration during a long stagnant dust event (Pan et al., 2015). In Beijing, due to synergistic effect of water soluble
97 substance at the surface of dust and relative humidity, the non-sphericity of dust particles even tent to be sphericalized (Pan
98 et al., 2017; Wang et al., 2017). The long-term observation on such effect was still lacking.

99 From November 15, 2016 to February 18, 2017, Beijing was consecutively suffered from several severe air pollutions with
100 hourly averaged mass concentration of $PM_{2.5}$ and $PM_{2.5-10}$ larger than $300 \mu\text{g}/\text{m}^3$ and $100 \mu\text{g}/\text{m}^3$. It provided a good chance to
101 investigate into the interaction between dust particles with pollutants. During this period, chemical composition, size
102 distribution, polarization properties of aerosol particles were concurrently measured, as well as vertical profile of
103 backscattering coefficient by Lidar at a downtown tower site of Beijing mega city. The objective of this study was to
104 investigate depolarization properties of aerosol particles in the polluted urban site on the single-particle basis, and to study the
105 impact of both water-soluble species and relative humidity (RH) on the morphological changes of dust particles. This study
106 will provide useful information in better understanding the physical and optical properties of particles in East Asia, and
107 improving numerical simulation on its environment/climate effect.

108 2 Observations

109 2.1 Observation overview

110 The field measurement was performed at a tower campus of Institute of Atmospheric Physics/Chinese Academy of Sciences
111 in the downtown area of Beijing mega city. The observation site located between 3rd North Ring road and 4th North Ring road,
112 where anthropogenic emissions are intensive in the daytime. Within the campus (150 m x 50 m), there is a 325 m tower for
113 meteorological measurement and scientific research; therefore anthropogenic activity nearby is limited. During the
114 observation period, a continuous dichotomous Aerosol Chemical Speciation Analyzer (ACSA-14) was placed on the roof of
115 two-story building in the campus. Polarization Optical Particle Counter was placed in air-conditioned room on the roof to
116 measure polarization properties of single particle less than $10 \mu\text{m}$. To avoid loss of particles in coarse mode, the sampled air
117 was drawn into the room by a supporting pump (flow rate: 10 lpm) through 2 m long 1/4-inch vertically assembled stainless
118 steel tube. From November 15 to December 15 2016, a UK-China joint field campaign, entitle as “In-depth study of air
119 pollution sources and processes within Beijing and its surrounding region (APHH-Beijing)” was also performed in the tower
120 campus. Detailed information about the objectives and instruments are shown in webpage (https://www.atmos-chem-phys.net/special_issue932.html).

122 2.2 Instruments

123 In this study, mass concentrations of particulate matter and water-soluble chemical compounds in both $PM_{2.5}$ and $PM_{2.5-10}$
124 were measured by ACSA-14 (KIMOTO electric Co. Ltd, Osaka, Japan) with 1-hour intervals at the observation site. The mass
125 concentration of particulate matter was determined using beta-ray absorption method. Mass concentration of SO_4^{2-} was



26 determined on the basis of BaSO₄-based turbidimetric method with addition of BaCl₂ dissolved in polyvinylpyrrolidone
27 solution. Mass concentrations of NO₃⁻ and water-soluble organic carbon were determined using ultraviolet absorption-
28 photometric method. Because mass concentration of NO₃⁻ was general high in Beijing, the instrument generally collected
29 aerosol samples in the first 5~10 minute in each hour and analyzed the samples in the rest time to guarantee follow Beer-
30 Lambert Law. The acidity of particles [H⁺], in unit of nmol/m³, was semi-quantitatively determined using pH-indicator
31 absorption-photometric method. The basic equation is $\text{pH}_{\text{solution}} = -\log [\text{H}^+ \times 10^{-6} + 10^{-4.6}]$, presuming that all the water-soluble
32 matter was dissolved in the extract liquid with pH value of 4.6. A factor of 10⁻⁶ was used to convert unit of [H⁺] from nmol/m³
33 to mol/L. The comparison of [H⁺] in PM_{2.5} between ACSA and off-line filter-pack measurement showed a good linear
34 correlation ($[\text{H}^+]_{\text{ACSA}} = 3.33 + 0.81 \times [\text{H}^+]_{\text{FP}}$) with $r^2 = 0.54$ (Personal communication with Prof. Osada in Nagoya University).
35 The details of the ACSA instrument are described in literature (Kimoto et al., 2013).

36 Depolarization ratio of single particle was determined using a Polarization Optical Particle Counter (POPC). POPC adopted a
37 780 nm linearly polarized laser beam to illuminate the aerosol particles that passed through measuring chamber vertically.
38 The direction of vibration of the electric field of the incident laser is parallel to the plane of the scattering angle. Detailed
39 information about POPC was described in literatures (Kobayashi et al., 2014; Pan et al., 2016; Pan et al., 2017). Forward
40 scattering signal at 60 degree respect to direction of incident light was measured by a photodiode with acceptance angle 45
41 degree to determine the size of particle. The backward scattering signal at 120 degree was split into P component (horizontal
42 with respect to the plane of the scattering angle) and S component. The depolarization ratio (DR) of the particles was defined
43 as the ratio of S component to P component (S/P). To avoid the coincidence error of the measurements, the inlet flow rate of
44 POPC was set to 80 ccm and was diluted with zero air (920 ccm, RH = 38 ± 1%). Overall measurement uncertainty in size
45 determination was less than 15%.

46 During observation period, the vertical structure of backscattering coefficient for aerosols was derived from Mie-scattering
47 Lidar system that installed at the same place of ACSA-14. This Lidar system, developed by the research group in National
48 Institute for Environmental Studies (NIES), employs a flash-lamp-pumped Q-switching Nd:YAG laser as the light source. It
49 emits pulsed lights with wavelength of 1064 nm and 532 nm with a frequency of 10 Hz, and collects the backscattered light
50 from the atmosphere by a 20 cm Schmidt-Cassegrain telescope. The light at 532-nm wavelength is also further separated into
51 S and P component (Sugimoto et al., 2002). The algorithm for classifying sphere and dust particles was described in literatures
52 (Shimizu et al., 2004; Nishizawa et al., 2011; Shimizu et al., 2017). To be note that, direct comparison of depolarization ratio
53 between POPC and Lidar system is difficult. Firstly, Lidar system receives backscattering light at almost 180 degree with a
54 field of view of 1 mrad; whereas POPC employs 120-degree backscattering signal. Secondly, Lidar system measures the total
55 volume depolarization from a volume of targeted air parcel; whereas depolarization properties from POPC is on a single
56 particles basis.



57 **2.3 Footprint analysis**

58 We simulated footprint region of aerosol particles at the observation site using NOAA Hybrid Single Particle Lagrangian
59 Integrated Trajectory (HYSPLIT) model (v4.9; available at <http://ready.arl.noaa.gov/HYSPLIT.php>). This model has been
60 widely applied into calculating long-range or meso-scales transport and footprint regions of air pollutions with fast
61 computational speed and high spatial resolution. HYSPLIT model is capable of forward/backward run in time to simulate the
62 dispersion/potential source of tracers in a given location. Detailed description and validations of this model was seen in
63 literature. In this study, input meteorological data of model is the product (GDAS dataset) of Global Forecast System (GFS)
64 from National Centers for Environmental Prediction (NCEP) with a spatial resolution of 0.5 by 0.5 degree, and a time-
65 resolution of 3 hours (0000, 0600, 1200 and 1800 UTC from data assimilation product; 0300, 0900, 1500 and 2100 UTC from
66 forecast model). By offsetting the release point by a meteorological grid point in the horizontal and 0.01 sigma units in the
67 vertical, ensemble simulation have 27 trajectories were calculated simultaneously in each hour, providing great advantage in
68 evaluate the uncertainty and potential footprint region. In the present study, the grids at which height of backward endpoint of
69 air parcel was less than the height of mixing layer was labeled as potential footprint region.

70 **3 Results and discussions**

71 **3.1 Overview in particulate matters and chemical species**

72 **3.1.1 Comparison of mass concentration of particulate matters**

73 Figure 2a shows the temporal variations of mass concentrations of ambient $PM_{2.5}$ that were measured by ACSA-14 at the
74 observation site. For comparison, mass concentration of $PM_{2.5}$ observed at a state-controlled monitoring station (Olympic
75 Centre, about 3 km northeast of the LAPC site) was plotted in the figure. In general, two results were in consistent well with
76 $r^2 = 0.8$, indicating that the pollution events were generally in regional scale with minor interference from emission sources
77 nearby. During observation period, number size distribution of ambient particles with optical diameter between $0.3 \mu m$ - 10
78 μm were measured with POPC, and the mass concentration of $PM_{2.5}$ was estimated assuming that all the particles were
79 spherical with a density of $1.77 g/cm^3$. Mass concentration of $PM_{2.5}$ estimated by POPC was compared well with ACSA-14
80 measurement before January 7, 2017, when ambient relative humidity (RH) was almost above 40%. Whereas estimated mass
81 concentration of $PM_{2.5}$ was underestimated obviously. One possible explanation is that, both air temperature and ambient RH
82 after January 7, 2017 decreased evidently. The interaction between water-soluble matters in $PM_{2.5}$ and moisture were unlikely
83 occurs, and the hypothesis of spherical shape of particles due to hygroscopic may resulted in relatively larger uncertainty in
84 estimating the optical size of particle on the basis of scattering light. Another possibility is that the chemical composition of
85 particles are different (discussed in section 3.1.2). As shown in Figure 2d, the northerly wind become stronger, which resulted
86 in larger proportion of mineral dust matters, the latter which have larger density ($2.2 - 2.8 g/cm^3$). Deploying the same density
87 for both particle in fine mode and coarse mode will lead to underestimation of total mass. It was pronounced for the case in
88 January 29, 2017 that observation site was subject to floating dust event with a hourly averaged mass concentration of PM_{10}



89 reached $734 \mu\text{g}/\text{m}^3$. Daily averaged mass concentration of $\text{PM}_{2.5}$ measured by ACSA-14 was $354.3 \mu\text{g}/\text{m}^3$, four times higher
90 than the values ($77.1 \mu\text{g}/\text{cm}^3$) estimated by POPC. Deployment of a larger particle's density of $2.8 \text{g}/\text{cm}^3$ only explain 35% of
91 the difference. Low detection limit of particle size of POPC was $0.5 \mu\text{m}$, and miscounting of particles less than $0.5 \mu\text{m}$ was
92 estimated to contribute another 10% of the difference. The most possible reason is that the irregularity of particles in fine
93 mode resulted in significant underestimating in particle diameter on the basis of scattering signal. However, the estimation of
94 spherical particles diameter by POPC bears smaller bias theoretically. For example, during a typical anthropogenic pollutant
95 dominant case on January 1, 2017, mass concentrations of $\text{PM}_{2.5}$ and PM_{10} was as high as 438.8 and $626.2 \mu\text{g}/\text{m}^3$, respectively.
96 Hourly averaged mass concentration of $\text{PM}_{2.5}$ estimated by POPC correlated well with ACSA-14 measurement with a ratio of
97 1.1 ± 0.1 . It was noticeable that $\text{PM}_{2.5}$ accounted for 80% of PM_{10} , and ambient relative humidity was 65%. It was implied
98 that anthropogenic water-soluble compounds in $\text{PM}_{2.5}$ underwent hygroscopic processes that may alter asphericity of the
99 particles (detail discussion in section 3.5).

100 Regarding the particles in coarse mode, mass concentration estimated by POPC is much better than that in fine mode. It was
101 because, firstly, the detection efficiency of POPC for the particles in coarse mode was better than that in fine mode, and
102 miscounting of particles in coarse mode by POPC was less likely to occur; secondly, interference of asphericity of particles
103 in coarse mode was insignificant in determining size of particle according to scattering signal. Besides, change in the refractive
104 index of particles due to mixing of mineral dust particles with anthropogenic pollutants (such as black carbon) also have
105 limited impact in size determination. In general, daily averaged mass fraction of $\text{PM}_{2.5-10}$ in PM_{10} ($\text{PM}_{2.5-10}/\text{PM}_{10}$) was ranging
106 $0.25 \sim 0.7$ (Supplementary Figure). The minimum value occurred in severe pollution days when daily averaged mass
107 concentration of $\text{PM}_{2.5}$ was larger than $250 \mu\text{g}/\text{cm}^3$ (Air Quality Level: VI), whereas $\text{PM}_{2.5-10}/\text{PM}_{10}$ ratio increased as mass
108 concentration of $\text{PM}_{2.5}$ decrease. It was because formation of secondary particulate matters (such as sulfate and nitrate) during
109 pollution episode was so overwhelming that make the contribution of mineral dust decrease, although mass concentration of
110 $\text{PM}_{2.5-10}$ increased. Number of studies have addressed the importance of mineral dust in promoting new particle formation (Nie
111 et al., 2012) and conversion of SO_2 to sulfate (He et al., 2012), both of which was related to formation of OH radical. However,
112 this study was performed in winter, role of mineral dust in the formation of regional pollution is out of scope of this study.

113 3.1.2 Chemical compounds in fine and coarse mode

114

115 In winter, nitrate, sulfate and water-soluble organic carbon (WSOC) were found in both fine mode and coarse mode (Figure
116 3). Mass concentration of nitrate in the fine (fNO₃) was $28.3 \pm 33.7 \mu\text{g}/\text{m}^3$ averagely with a maximum value of $190.9 \mu\text{g}/\text{m}^3$.
117 Mass concentration of nitrate in the coarse mode (cNO₃) was $2.9 \pm 4.8 \mu\text{g}/\text{m}^3$. The maximum value of cNO₃ ($43.1 \mu\text{g}/\text{m}^3$)
118 occurred at the different time from that for fNO₃, implying of complicated mass equilibrium of nitrate among different size
119 range. Table 1 summarizes the fNO₃/cNO₃ ratio as a function of mass concentration of $\text{PM}_{2.5}$ at RH > 40% and RH < 40%.
120 We found that, when ambient RH was less than 40%, fNO₃/cNO₃ ratio has a positive correlation with mass concentration of
121 $\text{PM}_{2.5}$, which demonstrated that nitrate mass preferentially formed in fine mode and mass transfer of nitrate toward coarse



mode was unlikely happen due to weak hygroscopicity of particles; However, when ambient RH was larger than 40%, fNO₃/cNO₃ ratio did not increase with PM_{2.5} concentration with a mean of 12.4 ± 6.5. The possible explanations were, first, once the aerosol phase nitrate formed in the fine mode, it absorbed water vapor simultaneously and grew larger; secondary, ambient nitric acid may directly stick on the surface of particles in coarse mode through heterogeneous processes; Although high concentration of PM_{2.5} in Beijing was regard as synergistic contributions from both local formation and long-range transport, it did not influence the fNO₃/cNO₃ ratio, at least in the present study.

Mass concentration of sulfate in the fine mode (fSO₄) and in the coarse mode (cSO₄) were 18.9 ± 24.8 μg/m³ and 2.2 ± 2.5 μg/m³ with maximum values of 143.1 μg/m³ and 25.2 μg/m³, respectively. As shown in Figure 3b, the variabilities of fSO₄ and cSO₄ concentrations have the same trend. fSO₄/cSO₄ ratio increased with mass concentration of PM_{2.5}, irrespective of ambient RH, because sulfate in the fine mode mainly formed via homogeneous reaction between sulfuric acid with ammonia. The positive correlation between fSO₄/cSO₄ ratio and RH indicated that water vapor also took effect in the formation of sulfate. It was worthy to note that, fNO₃/fSO₄ ratio varied among cases due to different air mass origin and meteorology condition. For instance, on Dec 21, 2016 (blue shaded strip in Figure 3), mass concentration of fNO₃ and fSO₄ were 122.4 μg/m³ and 74.1 μg/m³, with a fNO₃/fSO₄ ratio of 1.6; however on Jan 1, 2017 (red shaded strip in Figure 3), mass concentration of fSO₄ increased to 125.2 μg/m³ and fNO₃ decrease to 99.2 μg/m³ with a fNO₃/fSO₄ ratio of 0.79. Backward trajectory analysis for the case on Jan 1, 2017 showed that the air mass was mainly transport from North China Plain along Taihang Mountain, coal burning in NCP in winter may contribute to the sharp increase of fSO₄; however, for the case on Dec 21, 2016, the air mass was mostly stagnant near Beijing area, and the intensive emission of NO_x resulted in the large difference between fNO₃ and fSO₄. The variability of WSOC in both fine mode (fWSOC) and coarse mode (cWSOC) were consistent with fSO₄ with maximum values of 167.6 μg/m³ and 8.7 μg/m³ (Figure 3c).

Mass fraction of total water soluble matters (WSM) in PM_{2.5} and acidity of the particle are shown in Figure 3d. Here, WSM includes only SO₄²⁻, NO₃⁻, WSOC, and NH₄⁺, the latter of which was estimated on the basis of equation ($[NH_4^+] = 18 \times ([SO_4^{2-}]/96 \times 2 + [NO_3^-]/62 \times 2 - [H^+]/1000)$). In general, mass fraction of WSM in PM_{2.5} during pollution period was higher than that during clean period. On average, WSM/PM_{2.5} was 0.5 ± 0.16. We found that, WSM/PM_{2.5} was more likely related to origin and residence time of air mass than the ambient loading of PM_{2.5} concentration. For example, daily averaged mass concentration of PM_{2.5} reached the maximum (447.5 μg/m³) on Jan 1, 2017; whereas maximum value of WSM/PM_{2.5} (0.80) occurred on Jan 7, 2017 when the pollution period almost ended. On Jan 1, 2017 observation site was prevailing southwesterly wind which introduced pollutants from NCP where industrial emission was intensive; However, air mass was mostly from east region on Jan 7, 2017, and high concentration of cNO₃ (Figure 3a) and high RH (Figure 2d) indicated that heterogeneous processes played a key role. Mole concentration of [H⁺] in fine mode (fH⁺) correlate well with mass concentration of fSO₄ (Figure 3d), implying of possibility of presence of surplus of sulfuric acid that converted from SO₂ that emitted from coal burning during heating period.

154

155



156

157 Table 1 The relationship between fNO₃/cNO₃, fSO₄/cSO₄ and mass concentration of PM_{2.5} at different RH condition.

RH Classification	PM _{2.5} Classification	PM _{2.5} (μg/m ³)		fNO ₃ /cNO ₃ (unitless)		fSO ₄ /cSO ₄ (unitless)		RH (%)	
		Avg.	S.D.	Avg.	S.D.	Avg.	S.D.	Avg.	S.D.
RH<40%	<25	16.3	6.3	12.5	6.8	3.6	2.2	29.3	4.7
	25-50	37.5	7.2	15.1	7.2	4.7	1.9	32.3	5.9
	50-75	59.9	7.8	17.5	8.5	5.6	1.8	33.4	6.8
	>75	98.2	23.4	26.2	12.1	6.2	1.8	32.2	6.4
RH>40%	<50	33.4	13.1	12.1	6.1	4.5	1.8	53.3	14.1
	50-100	82.1	8.3	13.0	9.6	5.6	2.3	54.4	10.6
	100-150	119.2	14.5	9.5	5.3	6.1	3.4	60.2	10.1
	150-200	175.6	14.5	12.9	5.9	7.8	2.7	59.8	6.8
	>200	290.9	61.6	14.3	5.3	10.3	2.0	61.1	9.2

158

159 **3.2 Volume size distribution and depolarization ratio (δ)**

160 Volume size distribution of aerosols and averaged depolarization ratio (δ) during observation period are shown in Figure 4. In
 161 general, evolution of all the pollution cases were well captured by POPC. Volume size distribution of aerosols showed a
 162 pronounced peak at 1 μm, at which secondary anthropogenic pollutants were dominant. Correspondingly, δ value of particles
 163 were normally less than 0.1, consistent with the previous study in East Asia (Pan et al., 2016). On Nov 19, 2016, two peaks
 164 were observed at size range of 1 μm and 2~3 μm. δ value of particles at two size were as low as 0.1. Such pattern of volume
 165 size distribution has been described in previous study (Pan et al., 2015, 2016), which classified such phenomena as a mixing
 166 pollution type that both anthropogenic pollutants and mineral dust particles interacted. Five-day trajectory analysis indicated
 167 that air mass mainly originated from Mongolia Plateau and they were stagnant over East China for days (supplementary
 168 figure). Volume peak at size of 4~5 μm was not observed probably due to fast gravity settling of large particles in coarse mode
 169 during their stagnancy. On Nov 26, 2016, the observation site was influenced by floating dust, and volume size distribution
 170 had a pronounced peak at 4~5 μm, as expected. δ value of submicron particles also increased to 0.3, implying of the substantial
 171 presence of irregular mineral particles in the fine mode. From Dec 30, 2016 to Jan 8, 2017, it had a long-lasting pollution
 172 period in Beijing. Volume size distribution of aerosols varied due to impacts from both change in Planet Boundary Layer
 173 height and origin of aerosols. Multi-peak fitting analysis indicated that volume size distribution had two peaks with a dominant
 174 peak at size of 0.9 μm and another peak at size of 2 μm. Different from case on Nov 19, 2016, the δ values of particles were
 175 0.2~0.4, though ambient RH was the same (> 60%). It implied that chemo-physical properties of the particles were different,
 176 probably due to impact by mineral dust. Detailed discussion was in section 3.3.2.

177

178 **3.3 Variability of δ value for particles of different size**179 **3.3.1 δ value for particles in fine mode**

180 As pointed out in previous study, δ value generally depends on the size of particle (SF₂). Histogram analysis on the particles
 181 at size of 1 μm showed that there was one peak mode at a δ_{DP=1} value of 0.11; For the particles at size of 2 μm, a multi-



182 Gaussian fitting for frequency distribution of $\delta_{Dp=2}$ value showed there were one dominant peak at a value of 0.17 and a
183 shoulder value of 0.23, the latter of which was mostly related to the impact of dust event. We found that variability of $\delta_{Dp=2}$
184 value of particles in fine mode was a synergistic effect of both water-soluble inorganic matter (WSI) and RH. For example, in
185 Figure 5, $\delta_{Dp=2}$ value of particles decreased gradually from 0.3 to 0.1 as mass fraction of WSI in $PM_{2.5}$ increase from 0.2 to
186 0.65, and RH increased from 38% to 85%. It notes that, $\delta_{Dp=2}$ value decreased only when $RH > 60\%$ and mass fraction of
187 WSI > 0.6 . Mass fractions of both fSO₄ and fNO₃ in $PM_{2.5}$ showed a negative correlation with $\delta_{Dp=2}$ value with a slope of –
188 0.3 and -0.1, respectively. We speculated that fNO₃ might play a key role in decreasing of $\delta_{Dp=2}$ value of particles in the fine
189 mode because fNO₃ was accounting for ~50% of total WSI and deliquescent point of ammonium nitrate was ~60%, and the
190 impact of ammonium sulfate was less important since it started to undergo hygroscopic growth only at higher RH (79%).
191 Quantitatively distinguishing respective contribution of fNO₃ and fSO₄ on the decrease of δ value of particles was difficult
192 in the present study.

193

194 3.3.2 δ value of mineral dust aerosols

195 For the particles at size of 5 μm , histogram analysis of $\delta_{Dp=5}$ value had a wide range 0.3 - 0.55. Laboratory experiments on
196 typical spherical particles at a size of 5.124 μm (SS-053-P) showed that their $\delta_{Dp=5}$ value was 0.07 ± 0.01 . The larger $\delta_{Dp=5}$
197 value (> 0.3) of mineral dust particle in the ambient air indicated that they were aspherical in shape. Figure 6 showed time
198 variation of vertical profile of extinction coefficient of dust particles derived from ground-based Lidar observation. We can
199 see that there was a typical dust event on Dec 26, 2016 with a $PM_{2.5-10}/PM_{10}$ ratio of 68%, and extinction coefficient of dust
200 particles at site was larger than 0.3 Km^{-1} . $\delta_{Dp=5}$ value of dust particle was varying around 0.5, and no decrease of δ value of
201 dust particles was observed due to low cNO₃ concentration and low RH (Figure 6). Another dust impact case was from Jan
202 1, 2017 to Jan 7, 2017, we found that $\delta_{Dp=5}$ value of dust particles were apparently low with a mean value of 0.35. In particular,
203 during the period that mass concentration of cNO₃ increased up to $10 \mu\text{g}/\text{m}^3$ and ambient RH was ranging above 60%, hourly
204 averaged $\delta_{Dp=5}$ value of dust particles decreased to 0.2, implying that cNO₃ on the surface of dust particle may form as
205 $\text{Ca}(\text{NO}_3)_2$ owing to heterogeneous processes, and consecutive hygroscopic growth resulted in the decrease of its $\delta_{Dp=5}$ value.
206 Compared with the case on Dec 26, 2016, impact of this dust event was relative weak with a $PM_{2.5-10}/PM_{10}$ ratio of 27%. It
207 was worth noting that all the mineral dust impacting cases were captured by both Lidar and POPC observations, nevertheless,
208 the mixing state of mineral dust particles could be illustrated better with POPC measurement according to their $\delta_{Dp=5}$ variations.
209 Once the morphology of mineral dust particles was modified due to cNO₃ coating at high RH condition, Lidar observation
210 may underestimate the impact of dust due to decrease of $\delta_{Dp=5}$ value of particles. Such phenomena maybe more likely to
211 happen at the downstream of polluted area. For instance, dust particles were found to be spherical due to interaction with HCl
212 and HNO₃ at marine area (Tobo et al., 2012). Observations using POPC at Kyushu area of Japan also indicated that there was
213 a large amount of larger particles with a $\delta_{Dp=5}$ value between 0.05 ~ 0.15 when air mass came from NCP of China, implying
214 that the morphology of dust particles were altering with transport (Pan et al., 2015, 2016).



115

116 3.4 Footprint analysis of mineral dust particles

117

118 As discussed above, the decrease of $\delta_{Dp=5}$ value of mineral dust particles were influenced by both mass concentration of cNO_3
119 and ambient RH. We choose two mineral dust-influencing episodes to demonstrate the impact (Figure 7). Here, footprint
120 region of the air mass was calculated for the period that hourly averaged mass concentration of cNO_3 was higher than $5 \mu g/m^3$.
121 For the episode between Nov 24 and Dec 7 2016, the footprint region of air mass covered west of Inner Mongolia province
122 and South of Hebei province. The particles in coarse mode seemed to mostly related with anthropogenic dust (defined as dust
123 aerosols due to human activity, such as agriculture, industrial activity, transportation etc.) in NCP where NO_x emission and
124 atmospheric nitrate loading were also high. Averaged RH was relatively low with a mean value of 30% (Figure 7c). However,
125 for the episode between Jan 1 and Jan 8, 2017, averaged RH within the footprint region around NCP was as high as 60%
126 (Figure 7d), although mineral dust particle had similar origins. Adsorption of water vapour and consecutive heterogeneous
127 reaction lead to obvious decrease of $\delta_{Dp=5}$ value of mineral dust particles. It indicated that a synergetic effect of both nitrate in
128 coarse mode and high RH condition lead to morphological changes in dust shape. The variability of morphological changes
129 was simulated on the basis of T-matrix methodology and randomly oriented elongated ellipsoid particles. We found that
130 observed maximal $\delta_{Dp=5}$ value (0.5) of dust particle corresponded to an aspect ratio (defined as ratio of the longest dimension
131 to its orthogonal width) of 1.7. When δ value of mineral dust particles decrease to 0.2, the aspect ratio was estimated to be 1.5,
132 not being “spherical”. Therefore, we considered such dust particles as being ‘quasi-spherical’. Huang et al., (2015) pointed
133 out that layer-integrated δ value of anthropogenic dust particles in the PBL of NCP was lower than that of Taklimakan dust
134 on the basis of CALIPSO Lidar measurement, mostly due to mixed with other more spherical aerosol within the PBL. Because
135 Lidar observation just provide a averaged δ value of all the particle in the detecting volume, external mixing of dust particle
136 with substantial amount of secondary anthropogenic particles in spherical shape could also result in a low δ value. From view
137 point of this study, irregularity of anthropogenic dust particles in NCP were possibly the same as the nature dust in the source
138 region, however, their interaction in particular at high RH condition will obviously lead to decrease in δ value.

139

140 3.5 Impact of heterogeneous reaction on δ value of particles

141

142 As shown in Figure 8, δ value of particles decrease obviously with increase of mass fraction of water soluble Matters (WSM),
143 in particular at high RH condition. For the particles at $D_p = 2 \mu m$, their $\delta_{Dp=2}$ value was normally 0.3 when mass fraction of
144 WSM in $PM_{2.5}$ was less than 0.2, whereas it decreased to 0.1 when the mass fraction of WSM increased to 0.6, and RH also
145 increased to 80% (Figure 8a). The linear relation was because the growth of particles in fine mode was closely related to
146 formation of secondary inorganic matters (sulfate, nitrate, etc.) and organic aerosols. Throughout the atmospheric chemistry
147 processes, the positive feedback between aerosol and water vapor was ubiquitous. For example, hygroscopic processes of



148 anthropogenic secondary inorganic resulted in abundance of aerosol liquid water content, and the latter of which could provide
149 an efficient media of multiphase reaction which promote new particle formation, and so on. Therefore, the particles in $PM_{2.5}$
150 generally approach to spherical in shape, resulted in a low $\delta_{Dp=2}$ value, and the high RH and the high possibility that spherical
151 particles formed. The morphological changes of particles in $PM_{2.5}$ could be well simulated on the basis of T-matrix method
152 (Pan et al., 2017).

153 For mineral dust particles, As discussed, the $\delta_{Dp=5}$ value (0.3~0.5) was clearly higher than that of particle in fine mode because
154 of this high irregularity (Figure 8b). Since the mass concentration of cSO_4 and cNH_4 were insignificant in coarse mode, the
155 $\delta_{Dp=5}$ value was plotted versus mass fraction of cNO_3 in $PM_{2.5-10}$. Decrease of δ value of dust particles as a function of mass
156 fraction of cNO_3 in $PM_{2.5-10}$ was also obvious, especially when RH was high than 60%. Numbers of studies have reported
157 emission of anthropogenic dust in NCP was significant, and Calcium was the most abundant crustal element in NCP. We
158 believed that that $Ca(NO_3)_2$ present on the surface of mineral dust particles, and the decrease of $\delta_{Dp=5}$ value of particle in coarse
159 mode was mostly due to heterogeneous reactions and consecutive water-absorbing processes. Such kind of mineral dust
160 particles coated with anthropogenic pollutants have been observed by numbers of previous electro-microscopic studies
161 (literatures). Previous studies also demonstrated the presence of cSO_4 on the surface of dust particles, nevertheless, we think
162 the effect of cSO_4 on the decrease of $\delta_{Dp=5}$ value was negligible because the mass fraction of cSO_4 was tiny (<0.02) and the
163 $CaSO_4$ was hard to dissolve in limited amount of aerosol liquid water content. To note that, the chemical compounds (such
164 as kaolinite, illite, humic matters, etc.) of particles in coarse mode was very complicated, $\delta_{Dp=5}$ value just indicate a
165 synthetically effect of morphological changes as a result of all physical and chemical processes. To quantitatively characterize
166 their optical and environmental effect, detailed studies on $\delta_{Dp=5}$ value variability of one-fold compound in the laboratory was
167 still essentially need.

168 **4 Conclusions and implications**

169 Depolarization properties of aerosol particles is an important parameter classifying the aerosol types and describing the
170 variability of morphology of particles, which was related to complicated mixing processes and heterogeneous reactions. It
171 also has great impact on its transport and regional/global climate due to alteration of optical properties of particles. In 2017, a
172 field joint campaign (In-depth study of air pollution sources and processes within Beijing and its surrounding region, APHH-
173 Beijing) was performed at an urban site in Beijing mega city. One of key aims of the project is to assess the processes by
174 which pollutants are transformed through atmospheric chemical reactions. Taking this opportunity, we performed an online
175 observation on the depolarization ratio of single particles using a Polarization Optical Particle Counter. The chemical
176 compositions (SO_4^{2-} , NO_3^- , WSOC) and acidity of particles in both fine mode ($PM_{2.5}$) and coarse mode ($PM_{2.5-10}$) was
177 determined using a continuous dichotomous Aerosol Chemical Speciation Analyzer (ACSA-14). The main conclusions are as
178 follows: (1) Depolarization ratio (δ) of ambient particles generally increase with its size due to increase in irregularity of the
179 particles, and the characteristic values of δ for the particles at $Dp = 1 \mu m$ and $2 \mu m$ were 0.11, 0.17, respectively. Once the



180 observation site was influenced by dust event, both of δ values increased to above 0.3 due to presence of submicron mineral
181 dust particle in irregular shape. The δ value of the particles at $D_p = 2 \mu\text{m}$ was mainly determined by the mass fraction of water-
182 soluble inorganic matter in $\text{PM}_{2.5}$, in which water vapor was fully involved in their atmospheric formation processes. (2) In
183 NCP, anthropogenic dust was an important contributor to the atmospheric loading of particles, their δ values (0.2-0.3) were
184 found to be smaller than that (0.5) of nature dust because of adsorption of acidic substance (such as HNO_3) and coagulation
185 with water-soluble anthropogenic pollutants (nitrate, sulfate) and consecutive chemical reactions on the surface of dust.
186 Ambient relative humidity plays a key role in altering the morphology of mineral dust as a result of hygroscopic processes of
187 deliquescent substances such as $\text{Ca}(\text{NO}_3)_2$, in particular when $\text{RH} > 80\%$. In this study, we found that δ values of mineral dust
188 particle in NCP could be as smaller as 0.2, which could be termed as “quasi-spherical”. (3) We found that allocation of
189 anthropogenic pollutants in fine and coarse mode was influenced by the RH along the trajectories of air mass, and increase of
190 nitrate mass in coarse mode was highly associated with the dust event. It indicated that the mineral dust particles in NCP was
191 mostly coated with anthropogenic pollution, upon which classification and quantitative determination of anthropogenic dust
192 emission was possible, though a pioneering study have been done on the basis of satellite remote sensing and land type (Huang
193 et al., 2015).

194 In this study, we provided solid evidences in morphological changes of mineral dust particles in NCP. Variability of δ value
195 of particles is also a valuable parameter in distinguishing how mineral dust particle interacted with anthropogenic pollutants
196 in formation of regional-scale haze pollutions. This result also spurs us to revisit decades of Lidar observation data in better
197 describing the transport and vertical distribution of Asian dust and pollution, and its regional environmental effects under the
198 scenarios of China thirty years’ rapid urbanizations. A reliable optical model capable of discriminating multiple aerosol types
199 was necessary for detailed analysis of polarization-related remote sensing observations. This study suggested that an integrated
200 observation network with single-particle-based depolarization measurement was necessary for synthetically understanding
201 chemo-physical properties of Asian dust issue.

202 **Acknowledgements**

203 This work was supported by the National Natural Science Foundation of China (Grant No. 41675128 and 41571130034),
204 and in part supported by Chinese Ministry of Science and Technology (2016YFC0207904, 2017YFC0212402) and CAS
205 Information Technology Program (Grant No. XXH13506-302). The authors gratefully thank Prof. Kobayashi from
206 Yamanashi University and Prof. Yele Sun from State Key Laboratory of Atmospheric Boundary Layer Physics and
207 Atmospheric Chemistry/Institute of Atmospheric Physics for their valuable comments on the original manuscript.

208 **References**

209 Geng, F., Liu, Q., Chen, Y., Hua, Z., Mao, X.: Preliminary Study of Vertical Distribution of Aerosols during Dry Haze Periods around
210 Shanghai Based on CALIPSO, *Procedia Earth & Planetary Science*, 2, 217-222, 2011.



- 111 Hara, Y., Yumimoto, K., Uno, I., Shimizu, A., Sugimoto, N., Liu, Z., and Winker, D. M.: Asian dust outflow in the PBL and free atmosphere
112 retrieved by NASA CALIPSO and an assimilated dust transport model, *Atmospheric Chemistry and Physics Discussions*, 8, 8715-8742,
113 2008.
- 114 Hara, Y., Nishizawa, T., Sugimoto, N., Matsui, I., Pan, X., Kobayashi, H., Osada, K., and Uno, I.: Optical properties of mixed aerosol layers
115 over Japan derived with multi-wavelength Mie–Raman lidar system, *Journal of Quantitative Spectroscopy and Radiative Transfer*, 188, 20-
116 27, <http://dx.doi.org/10.1016/j.jqsrt.2016.06.038>, 2017.
- 117 Huang, J. P., Liu, J. J., Chen, B., and Nasiri, S. L.: Detection of anthropogenic dust using CALIPSO lidar measurements, *Atmospheric
118 Chemistry and Physics*, 15, 11653-11665, 2015.
- 119 Hofer, J., Althausen, D., Abdullaev, S., et al.: Long-term profiling of mineral dust and pollution aerosol with multiwavelength polarization
120 Raman lidar at the Central Asian site of Dushanbe, Tajikistan: case studies, *Atmospheric Chemistry & Physics*, 14559-14577, 2017
- 121 Kaufman, Y., Tanré, D., Boucher, O.: A satellite view of aerosols in the climate system, *Nature*, 419, 215-23, 2002.
- 122 Kim, J.-S., and Park, K.: Atmospheric aging of Asian dust particles during long range transport, *Aerosol Science and Technology*, 46, 913-
123 924, 2012.
- 124 Kimoto, H., Ueda, A., Tsujimoto, K., Mitani, Y., and Kimoto, T.: Development of a Continuous Dichotomous Aerosol Chemical Speciation
125 Analyzer, *Clean Technology*, 23, 49-52, 2013.
- 126 Kobayashi, H., Hayashi, M., Shiraiishi, K., Nakura, Y., Enomoto, T., Miura, K., Takahashi, H., Igarashi, Y., Naoe, H., and Kaneyasu, N.:
127 Development of a polarization optical particle counter capable of aerosol type classification, *Atmospheric Environment*, 97, 486-492,
128 2014. Muller, D., Ansmann, A., Mattis, I., Tesche, M., Wandinger, U., Althausen, D., Pisani, G.: Aerosol- type- dependent lidar ratios
129 observed with Raman lidar, *Journal of Geophysical Research Atmospheres*, 112, 2007.
- 130 Nishizawa, T., Okamoto, H., Sugimoto, N., Matsui, I., Shimizu, A., and Aoki, K.: An algorithm that retrieves aerosol properties from dual-
131 wavelength polarized lidar measurements, *Journal of Geophysical Research: Atmospheres*, 112, 2007.
- 132 Nishizawa, T., Sugimoto, N., Matsui, I., Shimizu, A., and Okamoto, H.: Algorithms to retrieve optical properties of three component aerosols
133 from two-wavelength backscatter and one-wavelength polarization lidar measurements considering nonsphericity of dust, *Journal of
134 Quantitative Spectroscopy and Radiative Transfer*, 112, 254-267, <https://doi.org/10.1016/j.jqsrt.2010.06.002>, 2011.
- 135 Nishizawa, T., Sugimoto, N., Matsui, I., Shimizu, A., Hara, Y., Itsushi, U., Yasunaga, K., Kudo, R., and Kim, S.-W.: Ground-based network
136 observation using Mie–Raman lidars and multi-wavelength Raman lidars and algorithm to retrieve distributions of aerosol components,
137 *Journal of Quantitative Spectroscopy and Radiative Transfer*, 188, 79-93, <http://dx.doi.org/10.1016/j.jqsrt.2016.06.031>, 2017.
- 138 Pan, X., Uno, I., Hara, Y., Kuribayashi, M., Kobayashi, H., Sugimoto, N., Yamamoto, S., Shimohara, T., and Wang, Z.: Observation of the
139 simultaneous transport of Asian mineral dust aerosols with anthropogenic pollutants using a POPC during a long-lasting dust event in late
140 spring 2014, *Geophysical Research Letters*, 42, 1593-1598, 2015.
- 141 Pan, X., Uno, I., Hara, Y., Osada, K., Yamamoto, S., Wang, Z., Sugimoto, N., Kobayashi, H., and Wang, Z.: Polarization properties of
142 aerosol particles over western Japan: classification, seasonal variation, and implications for air quality, *Atmospheric Chemistry and Physics*,
143 16, 9863-9873, 2016.



- 144 Pan, X., Uno, I., Wang, Z., Nishizawa, T., Sugimoto, N., Yamamoto, S., Kobayashi, H., Sun, Y., Fu, P., and Tang, X.: Real-time
145 observational evidence of changing Asian dust morphology with the mixing of heavy anthropogenic pollution, *Scientific Reports* (Nature
146 Publisher Group), 7, 1, 2017.
- 147 Quaas, J., Boucher, O., Bellouin, N., Kinne, S.: Satellite- based estimate of the direct and indirect aerosol climate forcing, *Journal of*
148 *Geophysical Research Atmospheres*, 113, 2008.
- 149 Ramanathan, V., Crutzen, P., Lelieveld, J., et al. Indian Ocean Experiment: An integrated analysis of the climate forcing and effects of the
150 great Indo- Asian haze. *Journal of Geophysical Research Atmospheres*, 106, 28371-28398, 2001.
- 151 Seibert, P., and Frank, A.: Source-receptor matrix calculation with a Lagrangian particle dispersion model in backward mode, *Atmospheric*
152 *Chemistry and Physics*, 4, 51-63, 2004.
- 153 Shimizu, A., Sugimoto, N., Matsui, I., Arao, K., Uno, I., Murayama, T., Kagawa, N., Aoki, K., Uchiyama, A., and Yamazaki, A.: Continuous
154 observations of Asian dust and other aerosols by polarization lidars in China and Japan during ACE-Asia, *Journal of Geophysical Research:*
155 *Atmospheres*, 109, 2004.
- 156 Shimizu, A., Nishizawa, T., Jin, Y., Kim, S.-W., Wang, Z., Batdorj, D., and Sugimoto, N.: Evolution of a lidar network for tropospheric
157 aerosol detection in East Asia, *Optical Engineering*, 56, 031219-031219, 2017.
- 158 Sugimoto, N., Matsui, I., Shimizu, A., Uno, I., Asai, K., Endoh, T., and Nakajima, T.: Observation of dust and anthropogenic aerosol plumes
159 in the northwest Pacific with a two-wavelength polarization lidar on board the research vessel Mirai, *Geophysical Research Letters*, 29,
160 2002.
- 161 Sullivan, R. C., Guazzotti, S. A., Sodeman, D. A., and Prather, K. A.: Direct observations of the atmospheric processing of Asian mineral
162 dust, *Atmospheric Chemistry and Physics*, 7, 1213-1236, 2007.
- 163 Thorsen, T., Fu, Q.: CALIPSO- inferred aerosol direct radiative effects: Bias estimates using ground- based Raman lidars, *Journal of*
164 *Geophysical Research Atmospheres*, 120, 12209-12220, 2016.
- 165 Tian, P., Zhang, L., Ma, J., Tang, K., Xu, L., Wang, Y., Cao, X., Liang, J., Ji, Y., Jiang, J. H., Yung, Y. L., and Zhang, R.: Radiative
166 absorption enhancement of dust mixed with anthropogenic pollution over East Asia, *Atmos. Chem. Phys.*, 18, 7815-7825,
167 <https://doi.org/10.5194/acp-18-7815-2018>, 2018.
- 168 Uno, I., Yumimoto, K., Shimizu, A., Hara, Y., Sugimoto, N., Wang, Z., Liu, Z., and Winker, D. M.: 3D structure of Asian dust transport
169 revealed by CALIPSO lidar and a 4DVAR dust model, *Geophysical Research Letters*, 35, 2008.
- 170 Uno, I., Eguchi, K., Yumimoto, K., Takemura, T., Shimizu, A., Uematsu, M., Liu, Z., Wang, Z., Hara, Y., and Sugimoto, N.: Asian dust
171 transported one full circuit around the globe, *Nature geoscience*, 2, 557-560, 2009.
- 172 Wang, Z., Pan, X., Uno, I., Li, J., Wang, Z., Chen, X., Fu, P., Yang, T., Kobayashi, H., and Shimizu, A.: Significant impacts of heterogeneous
173 reactions on the chemical composition and mixing state of dust particles: A case study during dust events over northern China, *Atmospheric*
174 *Environment*, 2017.



175 Winker, D. M., Vaughan, M. A., Omar, A., Hu, Y., Powell, K. A., Liu, Z., Hunt, W. H., and Young, S. A.: Overview of the CALIPSO
176 mission and CALIOP data processing algorithms, *Journal of Atmospheric and Oceanic Technology*, 26, 2310-2323, 2009.

177 Yu, H., Chin, M., Yuan, T., et al.: The Fertilizing Role of African Dust in the Amazon Rainforest: A First Multiyear Assessment Based on
178 CALIPSO Lidar Observations, *Geophysical Research Letters*, 42, 1984-1991, 2015.

179

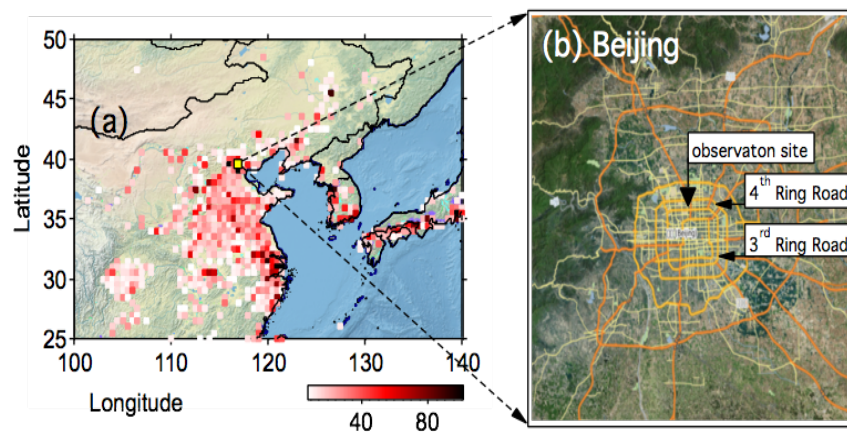
180



181

Figures

182



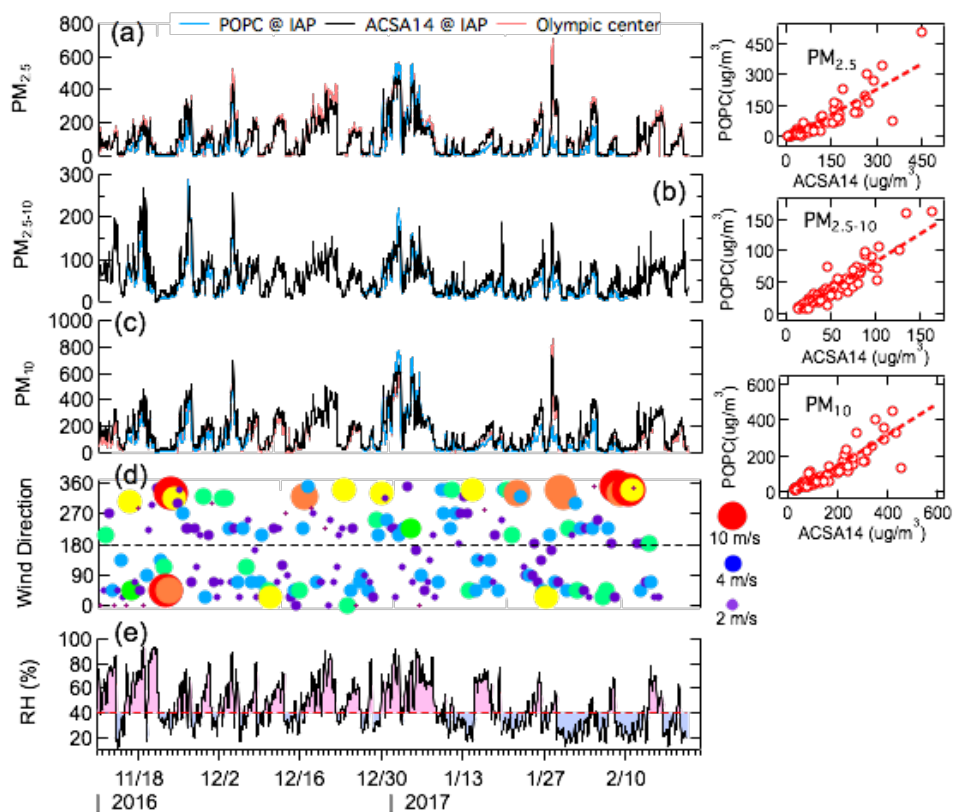
183

184 Figure 1. Geographic location of observation site and NO_x emission in East Asia (a), the transportation map of Beijing mega

185 city and location of tower campus of IAP.

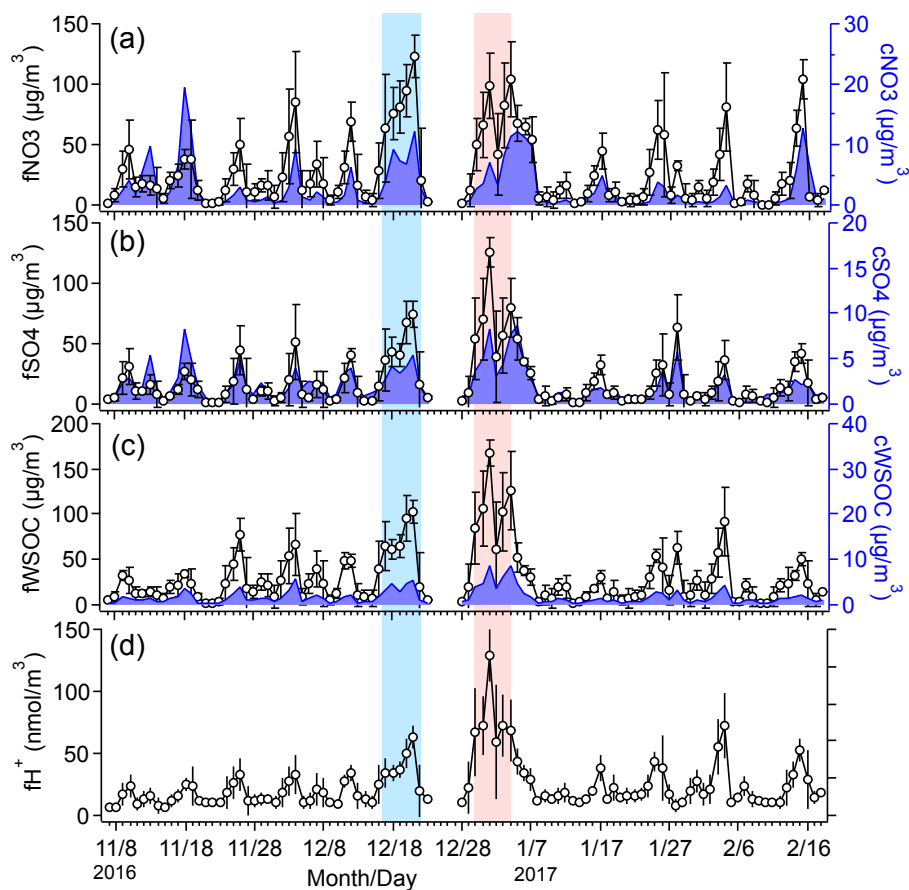


186



187 Figure 2. Temporal variation of mass concentration of PM_{2.5} (a), PM_{2.5-10} (b), PM₁₀ (c) measured by ACSA14 and derived
188 from POPC measurement, wind speed and direction (d) and relative humidity (e) at observation site. The three scatter plots in
189 the right indicate the linear relationship between ACSA14 and POPC, the correlations are $Y_{\text{POPC}} = -6.8 + 0.89 \times X_{\text{ACSA14}}$ ($r^2 =$
190 0.86), $Y_{\text{POPC}} = -19.5 + 0.84 \times X_{\text{ACSA14}}$ ($r^2 = 0.77$), $Y_{\text{POPC}} = -27.7 + 0.87 \times X_{\text{ACSA14}}$ ($r^2 = 0.81$) for PM_{2.5}, PM_{2.5-10} and PM₁₀
191 respectively.

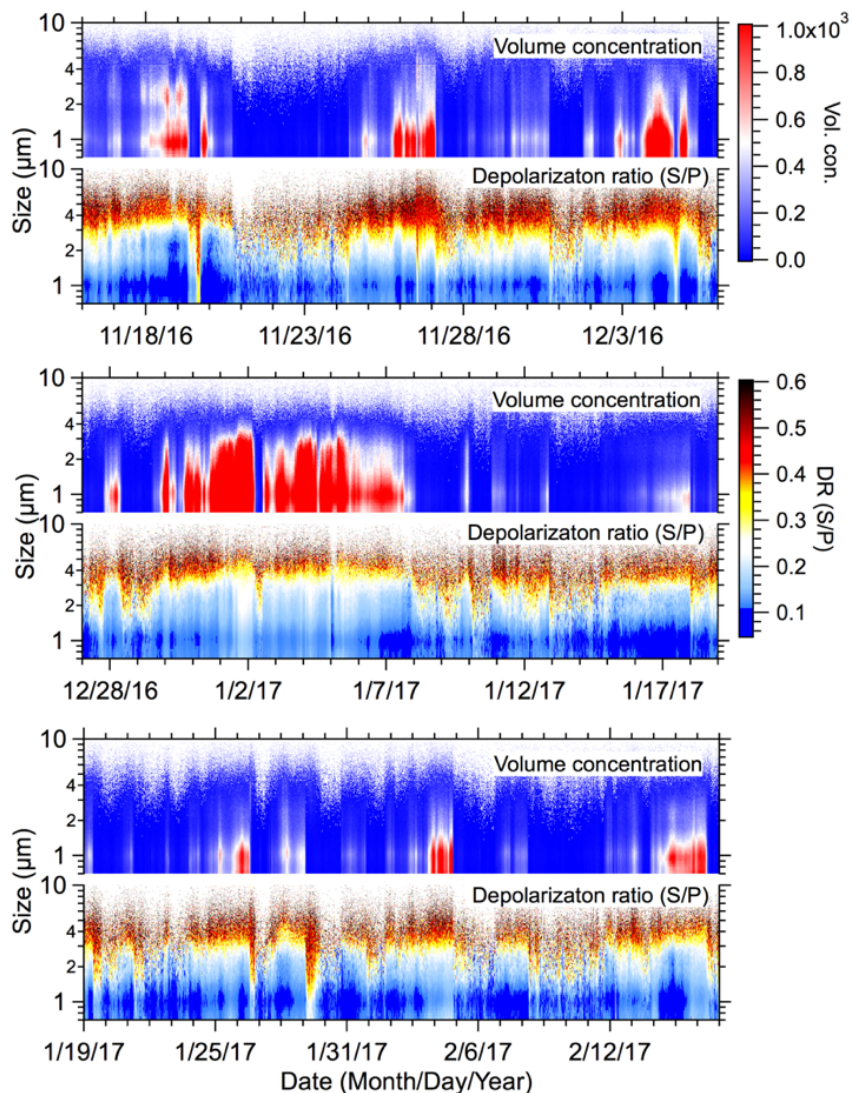
192



193

194 Figure 3 Temporal variations of mass concentrations of nitrate (a), sulfate (b) and water-soluble organic matters (c) in fine
195 mode and coarse mode, and acidity of particle (fH⁺) in the fine mode (d).

196

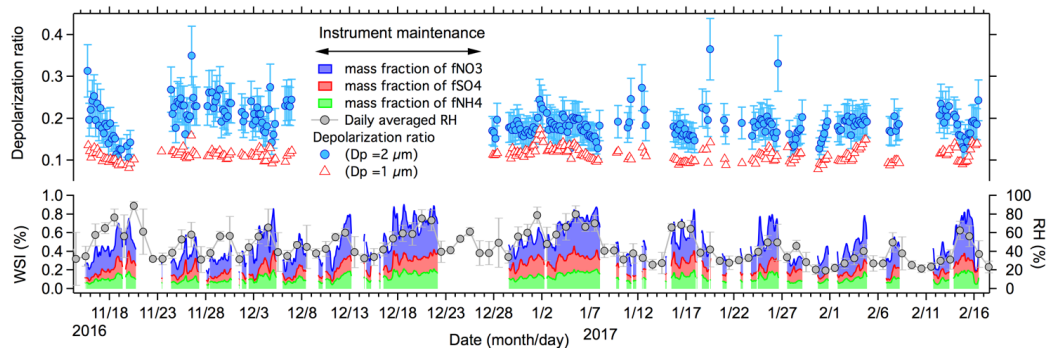


197 Figure 4 Volume concentrations of particles and corresponding depolarization ratio as a function of time during observation
 198 period. For better view the performance of the instrument, the observation results are shown in three-time slots.

199



500
501
502
503
504
505



506
507
508
509
510
511
512
513
514
515
516
517
518
519

Figure 5 Temporal variabilities of δ value for particles at size of $1 \mu\text{m}$ and $2 \mu\text{m}$ (a) and mass fraction of water-soluble inorganic matter (WSI, Blue: nitrate; Red: sulphate; Green: ammonium) in $\text{PM}_{2.5}$, ambient RH (b).

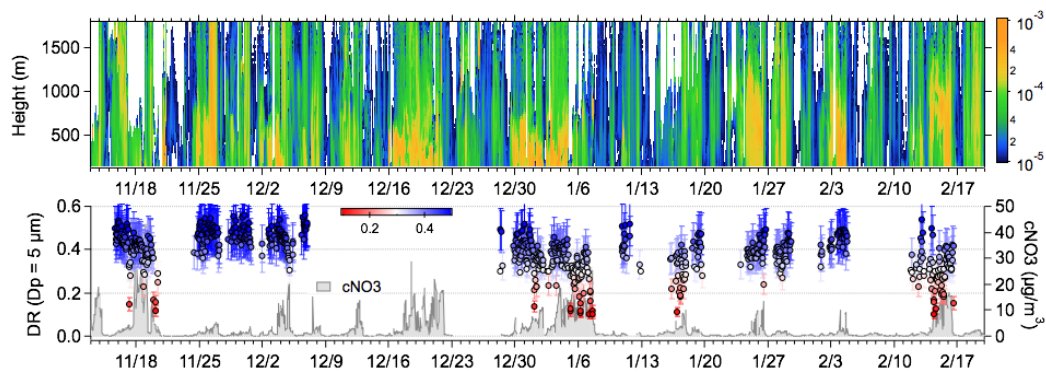


i20

i21

i22

i23



i24

i25 Figure 6 Vertical profile of extinction coefficient of dust particles derived from Lidar observation (a) and variability of δ

i26 value of mineral dust particles and NO_3^- in coarse mode aerosols (b) as a function of time. Here we choose the particles at a

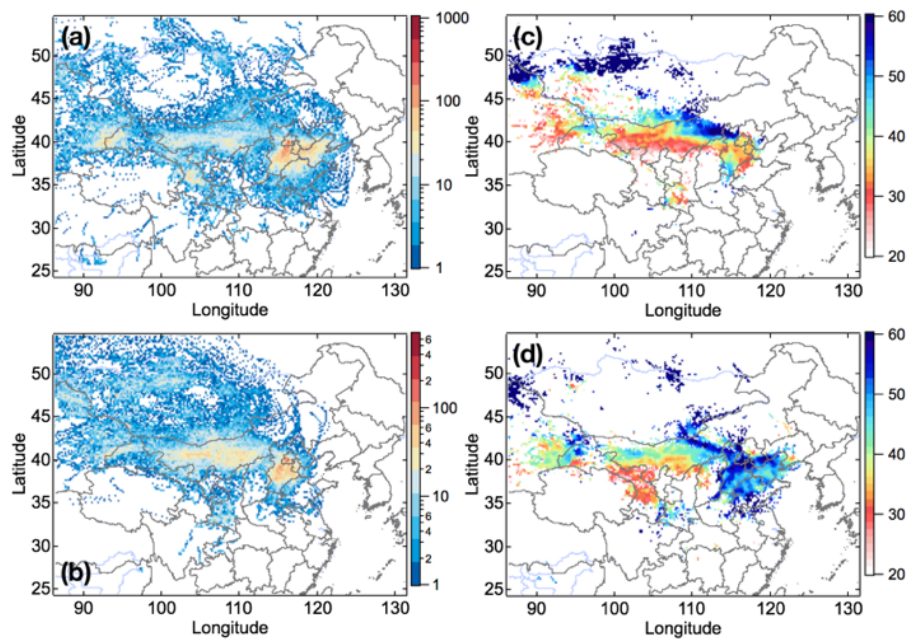
i27 size of $5 \mu\text{m}$ to indicate the mineral dust particles, marked as $\delta_{Dp=5}$ correspondingly.

i28

i29



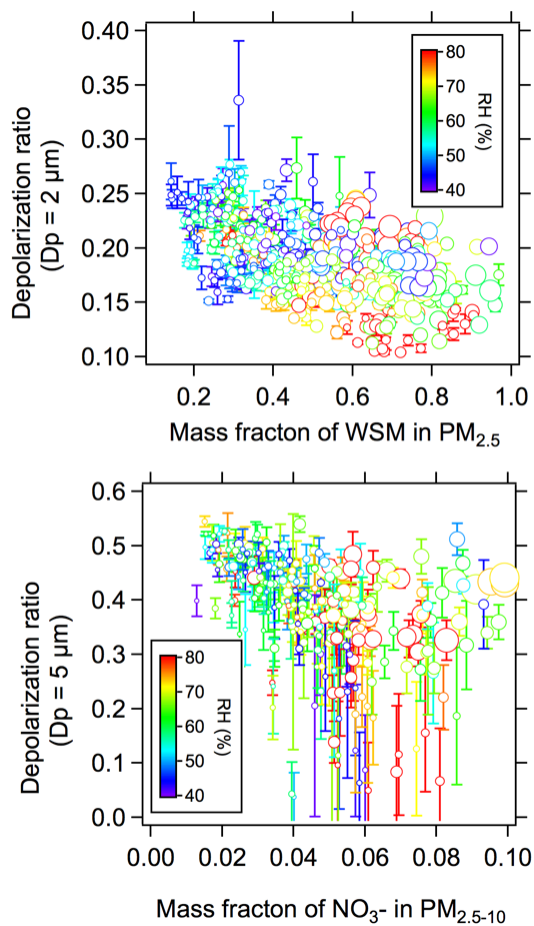
i30



i31 Figure 7 Footprint regions of mineral dust particles for the periods when averaged mass concentration of cNO_3 was higher
i32 than $5 \mu\text{g}/\text{m}^3$, while $\delta_{Dp=5}$ values were higher than 0.4 (a) and lower than 0.2 (b), and corresponding mean RH (c) and (d) in
i33 each grid within the footprint area on the basis of ensemble Hysplit analysis. Footprint height was defined as a height that
i34 endpoint of backward trajectory was lower than the height of mixing layer in that grid.

i35

i36



i37

i38 Figure 8 The variation of $\delta_{D_p=2}$ as a function of mass fraction of WSM in $\text{PM}_{2.5}$ (a), and $\delta_{D_p=5}$ as a function of mass fraction of

i39 cNO_3 in $\text{PM}_{2.5-10}$. The color represents the hourly averaged relative humidity during measurement.

i40

i41